SYNTHESIS AND CHARACTERIZATION OF HYDROCALUMITE: INFLUENCE OF AGING CONDITIONS ON THE STRUCTURE, TEXTURAL PROPERTIES, THERMAL STABILITY, AND BASICITY

THIAGO M. ROSSI, JUACYARA C. CAMPOS, AND MARIANA M. V. M. SOUZA * (iD)

[1]Escola de Química, Universidade Federal do Rio de Janeiro (UFRJ), Centro de Tecnologia, Bloco E, Sala 206, Rio de Janeiro, RJ CEP 21941-909, Brazil

Abstract—Hydrocalumite (HC) is a type of synthetic layered double hydroxide (LDH) that has many important industrial uses and is commonly synthesized by a co-precipitation method in a water:ethanol (2:3) mixture; however, atmospheric carbon dioxide interferes with the synthesis by decreasing the solubility of other gases in the reaction medium. The aim of the present study was to vary the temperature and aging time used in the coprecipitation method in order to mitigate the adverse effects of carbon dioxide. The water/ethanol mixture (2:3) was able to prevent atmospheric carbon dioxide contamination of the sample, as it decreased the solubility of the gas in the reaction mixture. Aging time (9–36 h) and temperature (35–95°C) were varied to modify the hydrocalumite structure, textural properties, thermal stability, and basicity. The characterization of the samples was performed using X-ray diffraction (XRD), X-ray fluorescence (XRF), Fourier-transform infrared spectroscopy (FTIR), nitrogen physisorption, thermogravimetric analysis (TGA), and CO_2 temperature-programmed desorption (TPD-CO_2) techniques. The aging time of 9 h and temperature of 95°C provided the most crystalline sample with the largest mean crystallite size (49 nm). The variation of the synthesis conditions also provided changes in the surface area (6.5–20.2 m^2 g^{-1}), pore diameter (116–148 Å), and pore volume (0.0147–0.0499 cm^3 g^{-1}). The temperature ranges for thermal decomposition of structural water and carbonate varied among the samples, indicating different thermal stabilities. The basicity (basic sites quantified by TPD-CO_2) was also affected by the change in aging conditions; the sample aged for 9 h at 65°C presented the greatest basicity (1557 μmol g^{-1}), whereas that aged for 36 h at 35°C had the least basicity (337 μmol g^{-1}).

Keywords—Aging · Hydrocalumite · Lamellar double hydroxide · Synthesis

INTRODUCTION

Hydrocalumite-like compounds (HLCs) are anionic clays that are part of the layered double hydroxide (LDH) family. LDHs bear a positive surface charge which attracts anionic species between the layers, where the layers contain two types of metals (Roy et al. 1992). The general formula of the HLCs is $[Ca_2M^{3+}(OH)_6]^+[(A^{n-})_{(1/n)}.mH_2O]^-$ where $A^{n-} = NO_3^-$, SO_4^{2-}, or CO_3^{2-} and $M^{3+} = Al^{3+}$, Fe^{3+}, Ga^{3+}, and/or Sc^{3+} (Leroux et al. 2002; Guo and Tian 2013; Barrado 2015; Sánchez-Cantú et al. 2015). The *c* lattice parameter varies with the size and charge of the interlayer anion, while the isomorphic substitution between calcium and aluminum is associated with the *a* lattice parameter (Pérez-Barrado et al. 2013).

The chemical and/or physical properties of LDHs differ from those of their individual elements because of a synergistic effect that occurs between the intercalated anions and the layered inorganic matrix. This effect is produced by its two-dimensional design (2D) (Prado et al. 2016). The LDH layered structure is joined by hydrogen bonds and electrostatic attractions between the layers (positively charged) and the interlamellar anions. The thickness of the lamellae is determined by the strength of the bonds between the hydroxyls of the layers and the anions, and the characteristics of the anion, such as orientation, number, and size (Cavani et al. 1991).

HLC with Ca^{2+}, Al^{3+}, and Cl^- ions, called hydrocalumite (HC) or Friedel salt, is easy to synthesize, with academic and industrial interest because of its potential for catalysis and metal adsorption. Hydrocalumite has a $Ca:M^{3+}$ molar ratio equal to 2 and formula $[Ca_2Al(OH)_6]Cl·2H_2O$. The structure consists of portlandite-like layers $[Ca(OH)_2]$ in which aluminum replaces some of the calcium. The metal cations in the layers have octahedral coordination and are positively charged $[Ca_2Al(OH)_6]$, and the interlayer space is occupied by water molecules and chloride anions (Terzis et al. 1987; Leroux et al. 2002; Guo and Tian 2013; Linares et al. 2014; Barrado 2015; Marsal et al. 2015; Sánchez-Cantú et al. 2015; Mao et al. 2017, 2018).

When calcined, hydrocalumite is converted into a calcium oxide (CaO) and mayenite ($Ca_{12}Al_{14}O_{33}$) mixture, giving it interesting basic properties and making it very useful in several applications, including in catalysts, catalyst supports, antacid agents, supercapacitors, adsorbents, environmental treatments, additives for polymers, cement, and ceramic pigments (Pérez-Barrado et al. 2013; Linares et al. 2014; Chen et al. 2016).

Various methods can be used to synthesize hydrocalumite. Urea hydrolysis employs urea as the precipitating agent, by which the LDH is formed from metal precipitation (heating can be used in this method), giving pure and well crystalline phases. Furthermore, the urea/metal ratio and metal concentration may be altered.

Another synthesis method is the sol-gel method, which yields high purity in the product and enables control of structural properties; this method consists of basic or acidic hydrolysis of the metal precursors. This methodology produces materials with thin layers and large surface area.
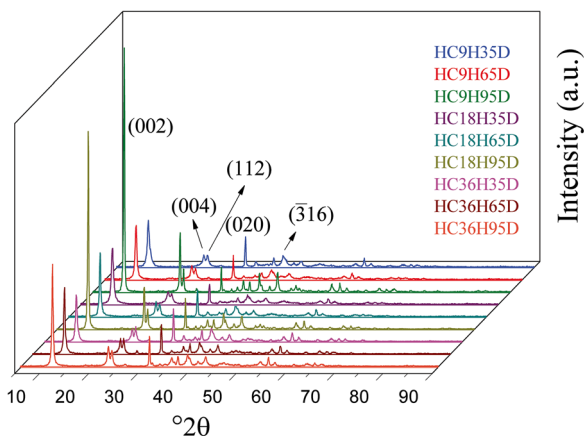
Fig. 1. X-ray diffraction profiles of the hydrocalumite samples

In the coprecipitation method, which consists of the addition of a solution containing inorganic salts over another of hydroxide, the metal hydroxides form brucite-like layers. Water molecules and anions are arranged in the interlayer spaces. The pH value is an important parameter for precipitation, and ideally is kept constant. Ions cannot precipitate if the pH is too low, so basic pHs are commonly used. Under high supersaturation conditions, several nuclei are formed and the resulting structures are of lower crystallinity. However, at low supersaturation, structures are formed with a high degree of crystallinity (Barrado 2015).

Coprecipitation is the most used method for LDH and HLC synthesis. Pfeiffer et al. (2011) synthesized a hydrocalumite-like compound ($[Ca_2Al(OH)_6]_2CO_3 \cdot mH_2O$) using an aqueous solution containing metal nitrate and another with potassium hydroxide and carbonate. López-Salinas et al. (1996) and Sánchez-Cantú et al. (2015) synthesized HLC ($[Ca_2Al(OH)_6]NO_3 \cdot mH_2O$) using NO_3^- as the charge-compensating anion. The nitrates were solubilized in decarbonated and deionized water while maintaining

the Ca/Al ratio of 2. Synthesis was carried out under helium flow to avoid sample contamination with atmospheric CO_2. Guo and Tian (2013) and Wu et al. (2010) synthesized HLC ($Ca_2Al(OH)_6Cl(H_2O)_2 \cdot mH_2O$) by adding dropwise a calcium and aluminum chloride solution (Ca/Al = 2) and a sodium hydroxide solution (2 mol L^{-1}) over a deionized water and ethanol solution (2:3 ratio). Ethanol reduces the CO_2 solubility so it prevents contamination of the hydrocalumite by carbonate. Literature regarding the effects of aging time and temperature on HLC synthesis, however, is scarce.

The purpose of the present study was, therefore, to determine the effects of aging time and temperature on the synthesis of hydrocalumite by means of the coprecipitation method, using a water/ethanol solution to prevent contamination from atmospheric CO_2, and to uncover the influence of synthesis conditions on the structure, textural properties, thermal stability, and basicity of the products.

EXPERIMENTAL

Hydrocalumite Preparation

The coprecipitation was based on the method of Guo and Tian (2013). All HCs were synthesized with a Ca/Al molar ratio of 2, as used in most other studies. In addition, synthesis was tested with other molar ratios (Ca/Al = 1, 3, and 4), but in addition to hydrocalumite, katoite ($Ca_3Al_2(OH)$) and portlandite ($Ca(OH)_2$) phases were formed. Therefore, the ratio of 2 was preferred. Three solutions were prepared using Sigma-Aldrich reagents (São Paulo-SP, Brazil): solution A containing the metal chlorides (1 mol L^{-1}); solution B containing sodium hydroxide (2 mol L^{-1}); and solution C containing water and ethanol (water/ethanol = 2:3). The precipitation was performed with the aid of a peristaltic pump (manufactured by Milan Equipamentos Científicos Ltda, Colombo, Paraná, Brazil) by which 100 mL of solution A and 100 mL of solution B were dripped simultaneously at a flow rate of 1 mL min^{-1}

Table 1. Lattice parameters and interlayer distance

Sample	Lattice parameter (Å)			Interlayer distance (Å)
	a	*b*	*c*	*D*
Theoretical*	9.853	5.715	16.898	7.771
HC9H35D	9.894(0.42)	5.737(0.38)	16.954(0.33)	7.764(0.09)
HC9H65D	9.893(0.41)	5.743(0.49)	16.966(0.40)	7.807(0.46)
HC9H95D	9.876(0.23)	5.743(0.49)	16.964(0.39)	7.759(0.15)
HC18H35D	9.895(0.43)	5.741(0.45)	16.944(0.27)	7.756(0.19)
HC18H65D	9.920(0.68)	5.741(0.45)	16.956(0.34)	7.796(0.32)
HC18H95D	9.894(0.42)	5.742(0.47)	16.940(0.25)	7.761(0.13)
HC36H35D	9.913(0.61)	5.738(0.40)	16.965(0.40)	7.760(0.14)
HC36H65D	9.876(0.23)	5.741(0.45)	16.939(0.24)	7.744(0.35)
HC36H95D	9.898(0.46)	5.738(0.40)	16.957(0.35)	7.731(0.51)

*From JCPDS 31-0245

The values in parentheses represent the amount by which the sample differs from the theoretical (Eq. 1).
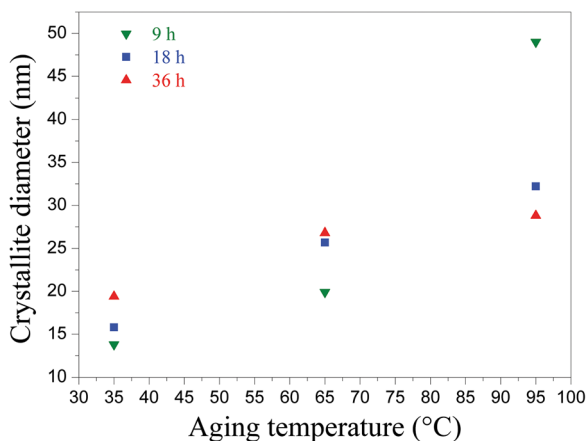
Fig. 2. Crystallite size as a function of aging temperature and time

Hydrocalumite Characterization

A Rigaku Miniflex II diffractometer with graphite mono-chromator (Rigaku Corporation, Kyoto, Japan) was used for powder X-ray diffraction (XRD) experiments (30 kV, 15 mA, CuKα radiation). The analysis was conducted over the range 5–90°2θ with a 0.05°2θ step using 2 s counting time for each step. The mean crystallite size was calculated in the stacking direction (direction *c*) with the Scherrer equation (Eq. 1) using the full width at half maximum (FWHM) of the peak corresponding to the (002) plane.

$$L = \frac{0.89\lambda}{\beta(\theta)\cos\theta} \qquad (1)$$

where $\beta(\theta)$ is the FWHM; θ, the Bragg angle; λ, the radiation wavelength; and *L,* the mean crystallite size.

X-ray fluorescence (XRF) was employed to determine the HC chemical composition, using Rigaku Primini equipment with a Pd tube (Rigaku Corporation, Kyoto, Japan).

Samples oven dried at 100°C were analyzed by Fourier-transform infrared (FTIR) spectroscopy using the KBr method (KBr:HC = 97:3) with a Shimadzu IRPrestige-21 spectrophotometer (Shimadzu Corporation, Kyoto, Japan) over the range 400–4000 cm^{-1}.

The Brunauer, Emmett, and Teller (BET) and Barret, Joyner, and Hallenda (BJH) methods were used to investigate the textural characteristics of the HCs. Specific surface area, average pore size, and pore volume were calculated from N_2 adsorption-desorption data acquired with a Micromeritics TriStar II 3020 device (Micromeritics Instrument Corporation, Norcross, Georgia, USA), operating at –196°C followed by outgassing for 24 h at 150°C.

Thermogravimetric analysis (TGA) was performed using a TA SDT Q600 thermogravimetric analysis device (TA Instruments, New Castle, Delaware, USA). 10 mg of sample was heated to 1200°C at 20°C min^{-1} in a 100 mL min^{-1} nitrogen flow. After the required temperature was reached, the sample was held at that temperature for 15 min. Chemical species released during heating were identified by analyzing the evolved gases with a coupled Pfeiffer PrismaPlus mass spectrometer (Pfeiffer Vacuum GmbH, Aßlar-HE, Germany). Masses m/e = 18 and 44, corresponding to H_2O and CO_2, respectively, were monitored. Enthalpy of decomposition was calculated using TA Universal Analysis software.

CO_2 temperature programmed desorption (TPD-CO_2) was carried out in a conventional device coupled to the Pfeiffer PrismaPlus mass spectrometer to quantify the HC basic sites. 150 mg of sample was pretreated at 150°C for 1 h under He flow (30 mL min^{-1}). CO_2 adsorption was performed for 30 min in a 40 mL min^{-1} flow rate of 10% CO_2/He at room temperature. Then the sample was exposed to He flow for 1 h to remove physically adsorbed CO_2. Finally, the TPD profile was recorded when the sample was heated at 20°C min^{-1} to 1000°C using He as the carrier gas at a 40 mL min^{-1} flow rate.
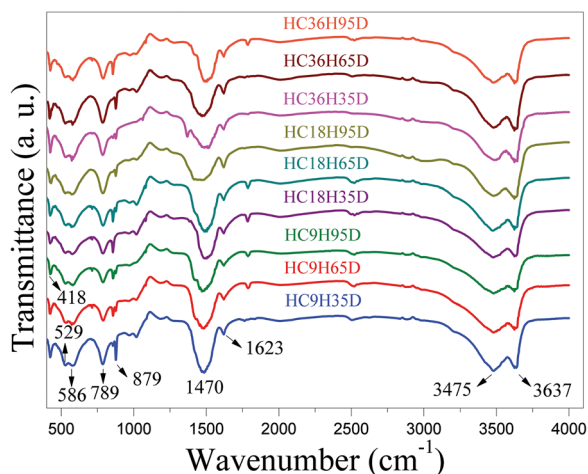
over 100 mL of solution C in a Teflon reactor with mechanical agitation. The pH of the reaction mixture was kept at 11.5 so that hydrocalumite could be formed.

After the pumping of solutions A and B was stopped, the gel formed in the reactor was stirred for a further 1 h to complete the precipitation. The suspension so formed was aged in an oven (Ethik Technology Equipment Solutions, Vargem Grande Paulista, São Paulo, Brazil) at 35, 65, or 95°C for 9, 18, or 36 h. The suspension was then vacuum filtered and washed with deionized water (90°C) to neutral pH. Finally, HCs were oven-dried at 100°C for 18 h, and after drying they were ground with a mortar and pestle. The sample names indicated the aging time and temperature, e.g. HC9H35D was aged for 9 h at 35°C. Sample HC36H65D was calcined in air flow (60 mL min^{-1}) at 200, 300, 400, 500, 600, 700, 800, and 1000°C for 120 min. The calcination aimed to reveal the phase transformations that occurred during the thermal analysis.

Table 2. Chemical composition of the hydrocalumite samples from XRF analysis

Sample	Molar fraction (%)			Molar ratio
	Ca^{2+}	Al^{3+}	Cl^-	Ca/Al
HC9H35D	57.1	26.4	16.5	2.16
HC9H65D	57.4	26.9	15.7	2.13
HC9H95D	57.5	27.3	15.2	2.11
HC18H35D	57.2	27.5	15.3	2.08
HC18H65D	56.5	28.9	14.6	1.96
HC18H95D	57.7	26.9	15.4	2.14
HC36H35D	56.5	28.5	15.0	1.98
HC36H65D	56.3	28.9	14.8	1.95
HC36H95D	56.9	27.1	16.0	2.10

Fig. 3. FTIR spectra

RESULTS AND DISCUSSION

Hydrocalumite with the chemical formula $Ca_4Al_2O_6Cl_2 \cdot 10H_2O$ (JCPDS 31-0245) was synthesized without the formation of secondary phases (Fig. 1). The water-with-ethanol mixture was mainly responsible for the avoidance of $CaCO_3$ formation in the sample because the CO_2 solubility was lower in the presence of alcohol. In addition, the decomposition of CO_3^{2-} to CO_2 was favorable in ethanol (Xu et al. 2011). The presence of fine and symmetrical peaks revealed that the samples were of good crystallinity (Jia et al. 2016). The structures formed were monoclinic, group $P21/c(14)$, and the reflections at 11.4, 22.9, 23.6, 31.3, and 39.1°2θ corresponded to the (002), (004), (112), (020), and ($\bar{3}16$) crystalline planes, respectively.

Zhang et al. (2012) investigated hydrocalumite synthesis using a nitrogen atmosphere (to avoid carbonation). Coprecipitation was carried out in the presence of ultrasound. During aging, conventional and microwave heating was used and reflux and autoclaving techniques were applied. However, because an inert atmosphere was used instead of an ethanol/water mixture, katolite formed as a secondary phase, demonstrating the deficiency in that method of synthesis.

The degree of crystallinity was judged by the intensity of the characteristic peak of the (002) plane. Aging the sample at 95°C for 9 h yielded the most intense peak and, thus, the greatest crystallinity, although it was not that much more intense than those from samples aged at 65 and 35°C; peaks from sample HC36H35D were slightly lower.

The unit-cell parameters and the interlayer distance were calculated from XRD patterns (Table 1) using the *Jade 5* XRD software. According to Pérez-Barrado et al. (2013), the *a* lattice parameter is related to the isomorphic substitution between the Al^{3+} and Ca^{2+} cations and *c* is related to the interlayer anion size and charge. The number in parentheses (Table 1, calculated by Eq. 2) indicates the amount by which the calculated value differs from the theoretical. This value was generally very small, showing that the calculated

values were close to the theoretical value. The parameters were similar among the samples because their stoichiometry was similar.

$$\% = \frac{|\text{theoretical} - \text{calculated}|}{\text{theoretical}} \times 100 \qquad (2)$$

The mean crystallite size was related to aging time and temperature (Fig. 2). The result evaluated the growth rate variation as a function of the aging conditions. According to Pérez-Barrado et al. (2013), the Scherrer equation is only sensitive to crystallite sizes smaller than 500 nm. Thus, crystallites with larger dimensions located in the lamellar plane were not detected by this method.
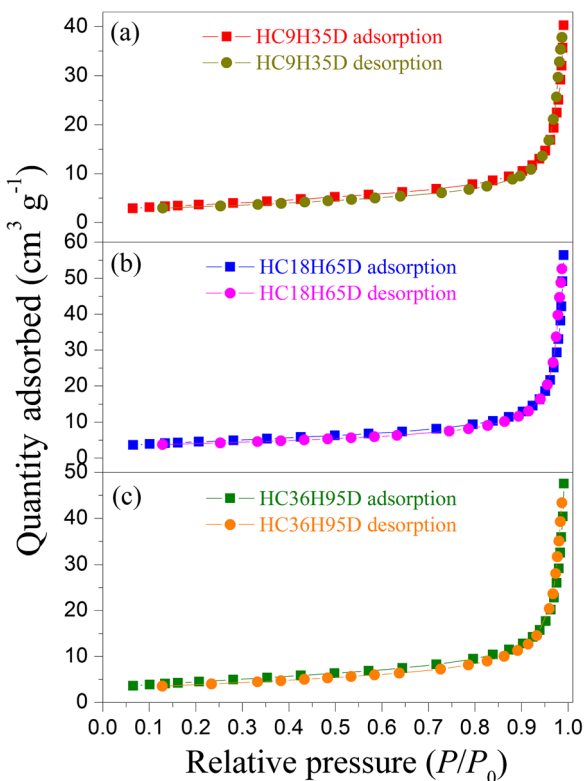
The crystal growth rate increased with increasing aging temperature (Fig. 2). The growth rate was greatest with 9 h of aging (13.8–49.0 nm), compared with 18 and 36 h. Shorter aging times were not tested. Aging at 35 and 65°C showed similar behavior in which the crystallite size increased proportionally with the aging time. At 95°C, however, the trend was the opposite; the diameter decreased with increasing aging time from 9 to 36 h. From among the conditions tested, aging for 9 h at 95°C was identified, therefore, as the optimum synthesis condition.

Calcium, aluminum, and chlorine molar fractions were similar for all samples, with the Ca/Al molar ratio close to the theoretical value of 2 (Table 2). Thus, the expected stoichiometry for hydrocalumite was reached. Based on the XRD and XRF results, synthesis by coprecipitation using a water/ethanol mixture was successful.

The FTIR spectra (Fig. 3) were characteristic of hydrocalumite (Domínguez et al. 2011; Pérez-Barrado et al. 2013; Sánchez-Cantú et al. 2016). The peak (Table 3) at 418 cm^{-1} was due to Ca–O vibrations. Bands centered at 529, 586, and 789 cm^{-1} were associated with the hydroxyl-to-metal (OH–metal) bonds. The narrow band at 879 cm^{-1} and the broad band at 1470 cm^{-1} were associated with the carbonate, indicating that the samples were partially carbonated. FTIR analysis was performed over a time period different from that used for XRD; after some time stored in a vacuum desiccator, the samples adsorbed CO_2 from the atmosphere. The carbonation did not occur during synthesis, but during storage, so the presence of a CO_2 band in the FTIR spectrum

Table 3. Identification of the IR bands representative of the synthesized hydrocalumites

Band identification	Wavenumber ν (cm^{-1})
Ca–O vibrations	418
Metal–OH bonds	529, 586, and 789
Carbonate band (bending non-planar)	879
C=O antisymmetrical stretching	1470
Distortion vibrations of water molecules	1623
OH stretching vibrations (CaO–H)	3475
OH stretching vibrations (AlO–H)	3637

Fig. 4. N$_2$ adsorption/desorption isotherms of samples **a** HC9H35D, **b** HC18H65D, and **c** HC36H95D

an ionic bond as a counterion to the hydrocalumite layer (positive charge) (Oladoja et al. 2014).

The N$_2$ adsorption-desorption isotherms of the samples (Fig. 4) were similar and classified according to IUPAC as type IV and type H3 hysteresis (slit-shaped pores), typical of a mesoporous material with pore diameters (Table 4) of 20–500 Å (Cota et al. 2010; Pérez-Barrado et al. 2013; Granados-Reyes et al. 2014). However, a very small fraction of macropores was present in the samples; above 0.96 relative pressure, a great increase in the amount of N$_2$ was observed, indicating the presence of macropores, which adsorbed was confirmed by the last point of the pore-size distribution (Fig. 5). The difficulty that N$_2$ molecules have in entering the interlayer space explains the small values for the BET surface area (Pérez-Barrado et al. 2013). Another factor that contributed to the reduction in surface area was the high hydrocalumite crystallinity (Granados-Reyes et al. 2014).

The N$_2$ physisorption analysis provided the results of total, micropore, and external BET surface areas (Table 5). The values in parentheses indicate the percentage of the total surface area attributable to the micropore and external surface areas. Hydrocalumites aged at 35 and 95°C showed larger BET surface areas after aging for 36 h, and at 65°C the largest surface area was achieved after 18 h. On the other hand, 9 and 18 h of aging at 95°C provided smaller BET surface areas, but for 36 h the area was less at 65°C. The increase in aging temperature promoted an increase in the fraction of the micropore surface area (Table 5), which consequently decreased the external surface area (only sample HC36H95D departed from this trend). Similarly, increasing the aging time tended to increase the micropore fraction and decrease the external surface area. Linares et al. (2016) and Prado et al. (2016) reported small surface area values (10.7 and 25.0 m^2 g^{-1}) for hydrocalumite, indicating agreement between values reported in the literature and those observed here (Table 5).

The pore distributions were unimodal with the most frequent pore diameter being in the range 22.4–31.1 Å (Fig. 5). From the N$_2$ physisorption analysis, the mean pore diameter (Table 4) was greater than the modal value because the mean value calculation took into account all distribution values and not just the most frequent value. The micropore and mesopore volumes were also acquired by N$_2$ physisorption analysis (Table 4). At 35°C the pore diameter was smaller after aging for 9 h, but at 65 and 95°C the smallest pore size occurred after

does not mean that the synthesis method failed to prevent hydrocalumite carbonation. The hydrocalumite carbonation during storage was also observed by Pérez-Barrado et al. (2013), Wen et al. (2015, 2016), and Linares et al. (2016).

The small band at 1623 cm^{-1} was attributed to bending vibrations of adsorbed H$_2$O. The band at 3500 cm^{-1} was assigned to O–H stretching vibrations of the H$_2$O coordinated to Ca^{2+} (3475 cm^{-1}) and Al^{3+} (3637 cm^{-1}). According to the literature, the 879 cm^{-1} band is probably associated with *M*–O lattice vibrations (*M* are metal atoms) (Zhang et al. 2012; Jia et al. 2016). The FTIR analysis was insensitive to chloride in the hydrocalumite structure because the chloride (negative charge) formed

Table 4. Average pore diameter and pore volume as a function of aging time and temperature

T_{aging} (°C)	D_{pore} (Å)			$V_{micropore}$ (cm^3 g^{-1})			$V_{mesopore}$ (cm^3 g^{-1})		
	t_{aging} (h)								
	9	18	36	9	18	36	9	18	36
35	119	148	146	0.0014	0.0014	0.0021	0.0263	0.0242	0.0499
65	147	137	119	0.0012	0.0021	0.0018	0.0240	0.0335	0.0237
95	132	141	116	0.0009	0.0010	0.0019	0.0174	0.0147	0.0308
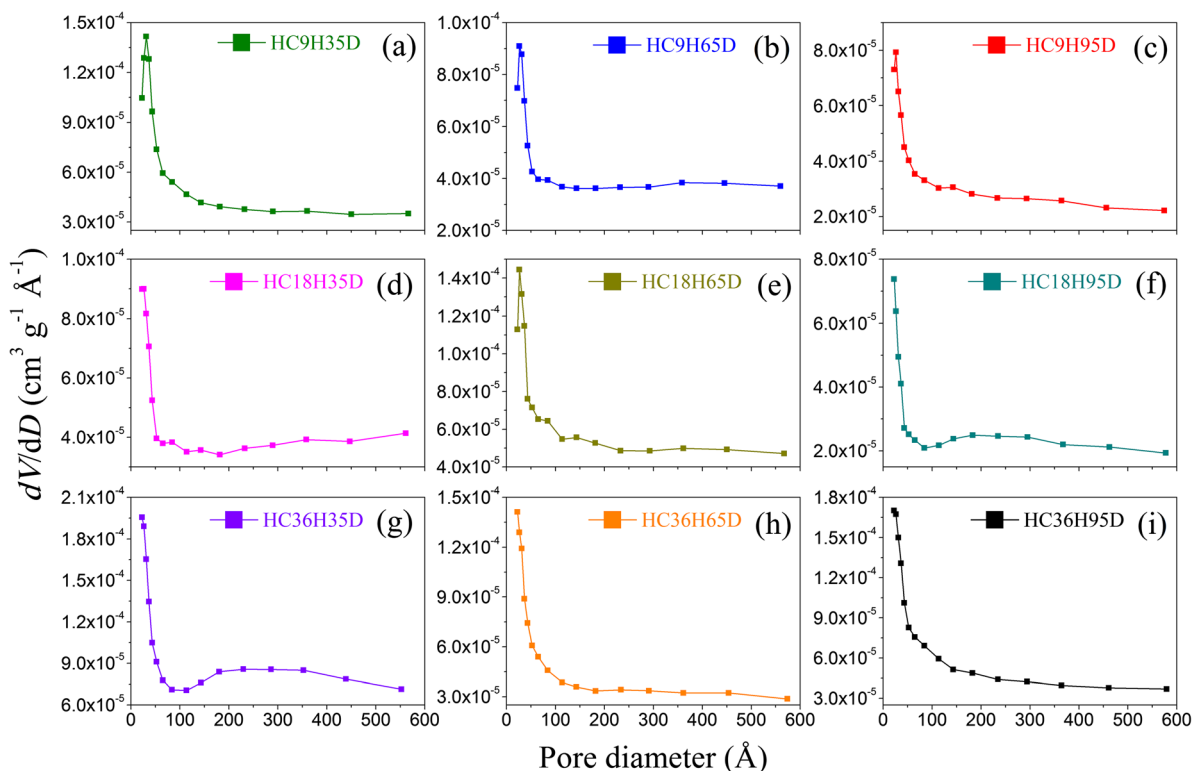
Fig. 5. Pore-size distribution of the samples: **a–c** 9 h, **d–f** 18 h, and **g–i** 36 h

36 h. The largest pore size after 9 h was achieved during aging at 65°C. However, for 18 and 36 h, the largest pore diameter was obtained at 35°C. Only at the aging temperature of 95°C was the pore size related to the BET surface area, in which the increase in pore diameter yielded a decrease in surface area. However, the surface area development was impaired by the high crystallinity; samples HC9H95D and HC18H95D had smaller surface areas because they were more crystalline (Figs. 1 and 2). The variation in the micropore and mesopore volumes followed the same trend as the total area variation, in which the volumes of both micropores and mesopores were larger in the samples with greater surface area. Nevertheless, the pore volume was small, which agrees with the literature (Granados-Reyes et al. 2014). The BET surface area can be related to the pore volume; the sample with the largest

mesopore volume had the largest surface area. Therefore, changes in aging conditions were able to modify the hydrocalumite textural characteristics.

The thermogravimetric analysis (TGA) curves highlighted mass loss with increasing temperature (Fig. 6). During the initial 30 min, samples were maintained at constant temperature (~35°C) in order to stabilize the DTG (Fig. 7) and DSC (Fig. 8) signals; during the subsequent 40 min, samples were kept at 1200°C to complete the last mass loss. All TG curves were similar, but some peculiarities can be highlighted. The TGA curves of samples aged for 9 h (Fig. 6a) showed that sample HC9H65D lost 7 wt.% in the non-heating step (~35°C); this stage was maintained under N_2 flow (100 mL min^{-1}). This weight decay may have been due to water removal by the flowing dry N_2. In the TGA curves of

Table 5. BET surface area (S) as a function of aging time and temperature

T_{aging} (°C)	S_{total} (m^2 g^{-1})			$S_{micropore}$ (m^2 g^{-1})			$S_{external}$ (m^2 g^{-1})		
	t_{aging} (h)								
	9	18	36	9	18	36	9	18	36
35	12.9	10.7	20.2	2.5(19)	2.7(25)	4.3(21)	10.5(81)	8.0(75)	15.9(79)
65	10.1	16.1	12.5	2.2(22)	4.2(26)	3.4(27)	7.9(78)	11.9(74)	9.1(73)
95	8.1	6.5	15.9	1.8(22)	2.0(31)	3.7(23)	6.3(78)	4.5(69)	12.3(77)

The values in parentheses represent the percentage of S_{total} accounted for by micropore or external surface area.

hydrocalumites aged for 18 h (Fig. 6b), sample HC18H35D lost ~2 wt.% in the step without heating. The profile for sample HC18H95D, however, was very different, with the first three stages producing a greater mass loss than the other stages. The TGA profiles of samples aged for 36 h (Fig. 6c) showed that sample HC36H95D lost 3 wt.% in the step without heating.

The total mass loss for the samples was between 39 and 41 wt.% (Table 6), with five decomposition stages, except in the case of sample HC36H95D (four stages). According to mass spectrometry coupled to thermogravimetric analysis (TG-MS, Fig. 9), the first mass-loss stage corresponded to decomposition of free water (~142°C); the second and third stages, to decomposition of lattice water and hydroxyl groups (~265–330°C and shoulder extending to ~550°C); the fourth stage, carbonate decomposition (712°C); and the fifth, chloride decomposition as hydrochloric acid (>1000°C). The calcium carbonate ($CaCO_3$) was converted to calcium oxide and CO_2 at 700°C (Hills 1968). The CO_2 present in the samples was, therefore, believed to be chemically bound to the hydrocalumites because its decomposition occurred at high temperature (712°C).

Mass spectrometry (MS) failed to detect HCl because the chloride concentration in the sample was below the equipment detection limit. At 887°C (Fig. 9), a shoulder was observed which could have been due to water (m/e = 18), but all water should have already been released by the time the sample reached this temperature. As this shoulder is within the temperature range of the last mass loss (815–1200°C, see Table 6), it is probably due instead to dehydroxylation of CaClOH, indicating that the chloride may also have been converted to HCl or Cl_2. For sample HC36H95D, decomposition stages

corresponded to release of (1) free water, (2) lattice water, (3) carbonate, and (4) hydrochloric acid.

TG curves of hydrocalumites presented by Zhang et al. (2012) indicated three mass-loss stages, with a total loss of 40–49 wt.%, which, according to those authors, is typical of hydrocalumites containing chlorine. The three stages were: (1) 90 to 200°C – free and lattice water, (2) 200 to 400°C – hydroxyl present in the double hydroxide layer, and (3) 400 to 1000°C – chloride that is converted to HCl (Zhang et al. 2012). Domínguez et al. (2011) also performed thermogravimetric analysis on hydrocalumites, and observed a total mass loss of 39–42 wt.%, where water was removed in two stages, the first at 120°C (13 wt.%) and the second at 310°C (16 wt.%). Chloride was removed (8 wt.%) as hydrochloric acid at temperatures >1000°C. These thermogravimetric analysis results agree, therefore, with other published literature.

The mass loss in the first stage was less for the first five hydrocalumites (Table 6), which indicated lower hydration of these samples. In addition, all samples had a greater lattice water fraction than free water; the sum of stages 2 and 3 was larger than the stage 1 fraction (for HC36H95D the stage 2 fraction was greater than that for stage 1). Looking at the second and third stages, the first five samples had a greater mass loss in the second stage, whereas for samples HC18H95D, HC36H35D, and HC36H65D the third stage had a greater mass loss. This can be related to the temperature range of each stage. When the temperature variation was greater, the mass loss was also greater. Therefore, the results were consistent, where the lattice water was decomposed at higher temperatures because it was more strongly linked to the material structure.

The sample that presented the largest mass loss due to carbonate decomposition (stage 3) was HC36H95D, with a loss of ~16.5 wt.%, followed by samples HC9H35D and HC18H65D (Table 6). On the other hand, much less carbonate was evolved from samples HC18H95D, HC36H35D, and HC36H65D (7.2, 9.2, and 8.4 wt.%). These features of this material were interesting in terms of CO_2 capture and sequestration, as reported by Rossi et al. (2019).

The chloride decomposition fraction (stage 4 for HC36H95D and stage 5 for the others) varied slightly among the samples (5.1–6.9 wt.%), which was expected because chloride cannot be captured out of the environment as can water and CO_2.

The free water was released from the samples between 35 and 169°C (Table 6). The lattice water was released over five different temperature ranges depending on the sample: (1) 169–453°C for HC36H95D, (2) 169–499°C for HC9H35D and HC18H65D, (3) 169–524°C for HC36H35D, (4) 169–550°C for HC18H95D and HC36H65D, and (5) 169–604°C for samples HC9H65D, HC9H95D, and HC18H35D. The high temperature required to release the lattice water pointed to a strong interaction of the water molecule with the material structure and of hydroxyl with the lamellae cations. Kuwahara et al. (2012) also assumed greater interaction of the hydroxyl groups with cations when the hydroxyl decomposition temperature was higher.
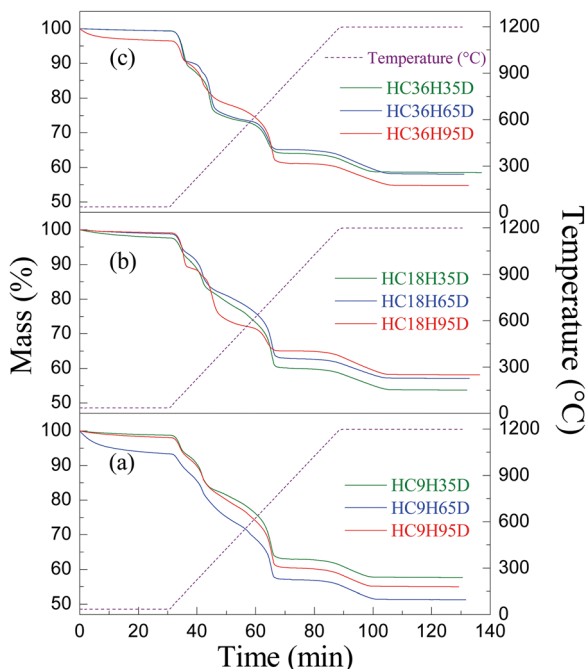

Fig. 6. Thermogravimetric analysis of the samples aged for **a** 36 h, **b** 18 h, and **c** 9 h

The carbonate decomposition as CO_2 also occurred over five temperature ranges, depending on the sample: (1) 453–815°C for sample HC36H95D, (2) 499–815°C for HC9H35D and HC18H65D, (3) 524–815°C for HC36H35D, (4) 550–815°C for HC18H95D and HC36H65D, and (5) 604–815°C for samples HC9H65D, HC9H95D, and HC18H35D. Similarly, as reported for water, the carbonate interacted more strongly with the material structure (forming $CaCO_3$), as evidenced by the high decomposition temperature. Chloride was released as HCl at 815–1200°C in all samples.

Typical DTG curves revealed five (Fig. 7a–h) and four (Fig. 7i) well defined peaks. Mass losses were related to the peaks of these curves, in which larger peaks indicated larger mass losses, corroborating the results presented previously (Table 6). From the DTG curves, the mass-loss regions, temperature ranges, and integration limits were identified accurately, and were needed to calculate the heat involved in each mass-loss region of the DSC curve (Fig. 8).

Downward DSC peaks (Fig. 8) represented endothermic events and one upward peak an exothermic event. Domínguez et al. (2011) reported endothermic events for water decomposition and exothermic events for chloride decomposition. The DSC curves showed overlapping peaks at stages 3 and 4 (Fig. 8a–e) and at stages 1, 2, and 3 (Fig. 8f–h). For the overlapping peaks, the integration to calculate the heat was made considering the entire region of the peaks. For example, in the peak corresponding to stages 3–4 (Fig. 8a), the two peaks were

integrated together, i.e. the heat of sample HC9H35D for stage 3 (Table 6) corresponded to the heat involved in stages 3 and 4. Therefore, an empty space was placed in stage 4. In reality, the value 805 kJ kg^{-1} referred to stages 3 and 4. The heat was not calculated separately because the endothermic peak of stage 3 was not well defined; this situation was repeated for all overlapping peaks.

In the samples aged for 9 h (samples HC18H35D, HC18H65D, and HC36H95D; Table 6), the heat absorbed to release all free water and part of the lattice water (534–849 kJ kg^{-1}) was calculated in the same integration, but as the mass-loss fraction of the second stage accounted for ~64–72 wt.% of the first two stages, the heat involved in the second stage represented the largest fraction (~68%) of that heat. Note that samples HC9H35D and HC36H95D presented the largest and smallest amounts of heat absorbed in stages 1 and 2 (849 and 534 kJ kg^{-1}), respectively, which infers that water interacted more strongly with the material structure in sample HC9H35D than in sample HC3H95D. On the other hand, the heat absorbed to release all water (1032–1479 kJ kg^{-1}) from samples HC18H95D, HC36H35D, and HC36H65D, calculated using the first three mass-loss stages, revealed that the loss of lattice water (second and third stages) accounted for ~58–65 wt.% of the three stages and the heat involved in the lattice water decomposition was ~62 wt.%, indicating that water was bound more strongly to hydrocalumite in sample HC36H65D than in the other samples.
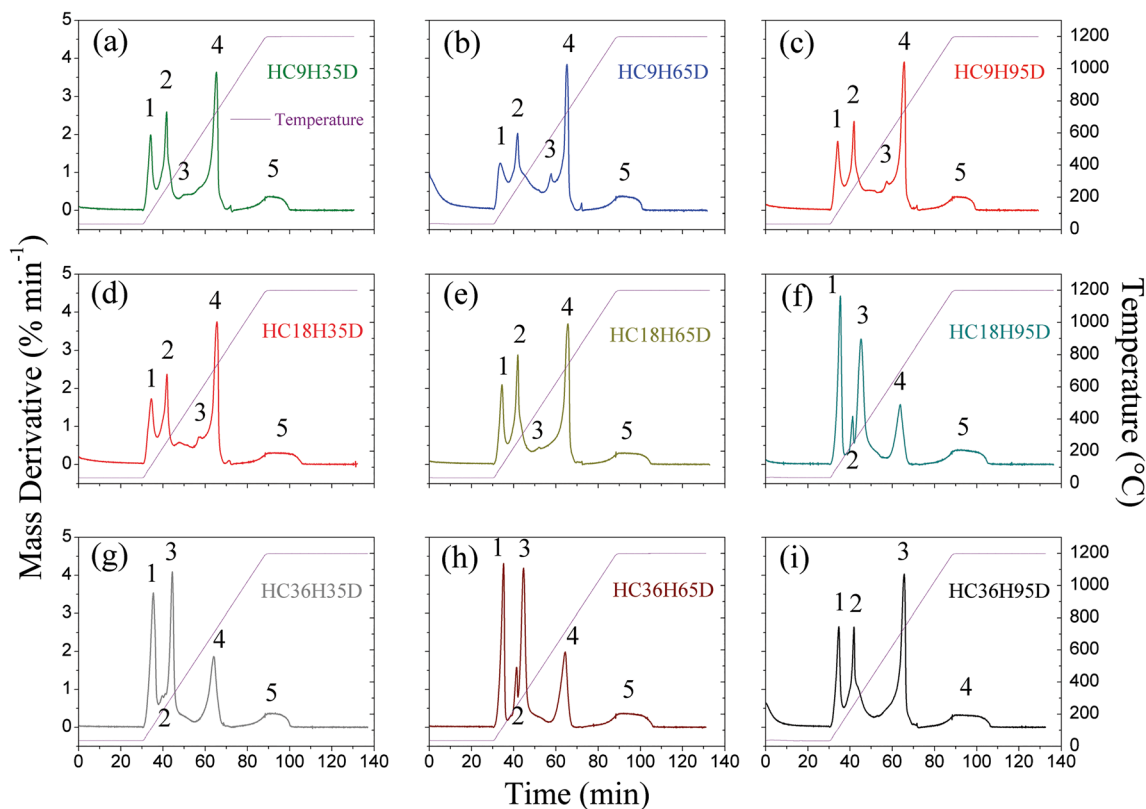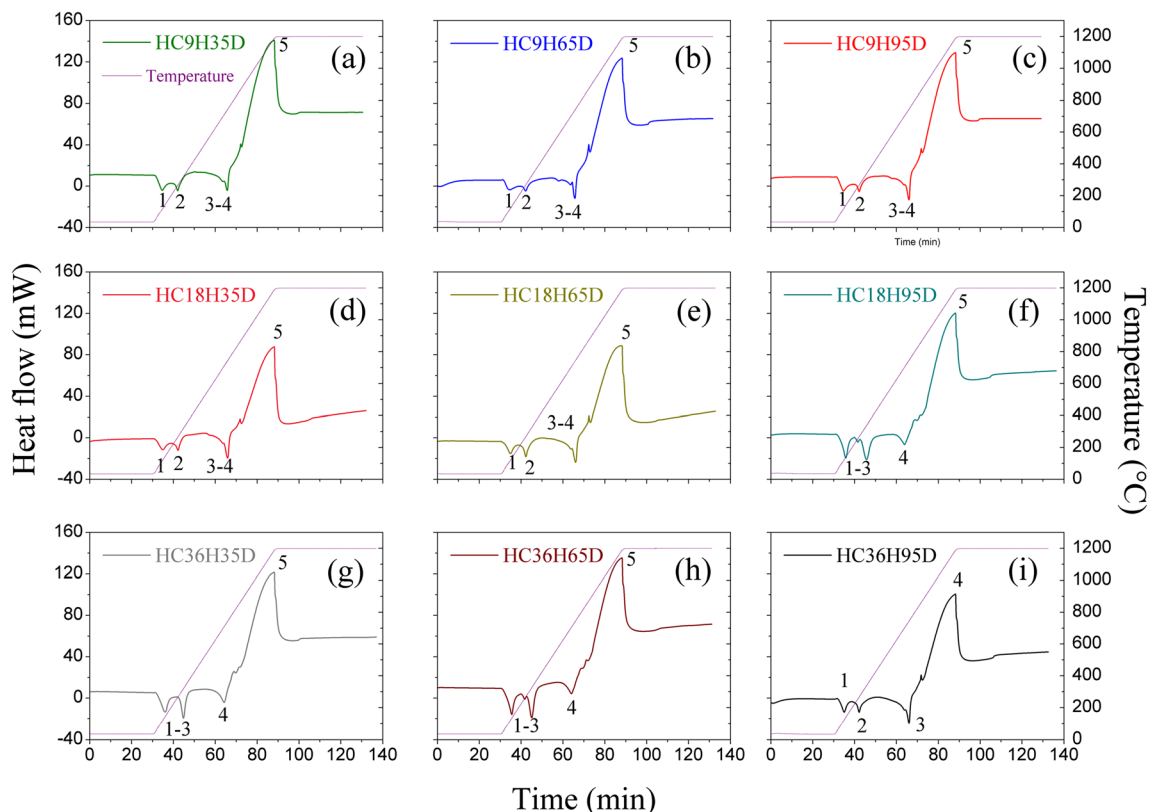

Fig. 7. Derivative of weight (DTG) over time for samples aged for **a**–**c** 9 h, **d**–**f** 18 h, and **g**–**i** 36 h

Fig. 8. Differential scanning calorimetry (DSC) analysis over time for samples aged for **a–c** 9 h, **d–f** 18 h, and **g–i** 36 h

The DTG peak of the third stage was very small (Fig. 7a–e), indicating a small mass-loss fraction (Table 6). As mentioned previously, in this sample group the heat was calculated by integrating the DSC curve region of stages 3 and 4 because the third endothermic peak was not well defined (superimposed on peak 4). However, the mass-loss fraction for stage 4 was large, ranging from 75 to 89 wt.%

(Fig. 7a–e). Based on this, one may assume that the heat absorbed in the third and fourth stages of mass loss (646–856 kJ kg^{-1}) is predominantly associated with carbonate decomposition. For sample HC18H95D and those aged for 36 h, the fourth stage and the third stage (HC36H95D) (Fig. 8f–i) were related integrally to the heat absorbed by the carbonate decomposition. Sample

Table 6. Study of thermal decomposition of hydrocalumites: temperature range, mass loss, and heat of decomposition

| Sample	Temperature (°C)					Weight loss (%)					Heat (kJ kg^{-1})				
	Stages														
	1	2	3	4	5	1	2	3	4	5	1	2	3	4	5
HC9H35D	35–162	162–366	366–499	499–824	824–1200	5.6	9.9	2.6	16.0	5.1	849	805			−7197
HC9H65D	35–173	173–496	496–612	612–815	815–1200	5.6	14.3	3.9	12.0	5.6	650	726			−6302
HC9H95D	35–168	168–482	482–598	598–812	812–1200	5.7	12.8	3.4	13.7	5.2	703	856			−5974
HC18H35D	35–167	167–502	502–603	603–806	806–1200	5.9	13.3	3.0	13.1	6.0	606	646			−4708
HC18H65D	35–164	164–397	397–499	499–812	812–1200	5.6	11.0	2.0	15.9	5.6	638	842			−5328
HC18H95D	35–178	178–266	266–547	547–812	812–1200	10.0	2.5	14.2	7.2	6.8	1099			570	−5718
HC36H35D	35–181	181–255	255–524	524–824	824–1200	10.7	2.8	12.0	9.2	5.3	1032			712	−5847
HC36H65D	35–162	162–267	267–553	553–815	815–1200	8.8	3.3	13.4	8.4	6.9	1479			433	−5895
HC36H95D	35–164	164–453	453–815	815–1200		6.5	11.9	16.5	6.4		534	971	−5385	−	
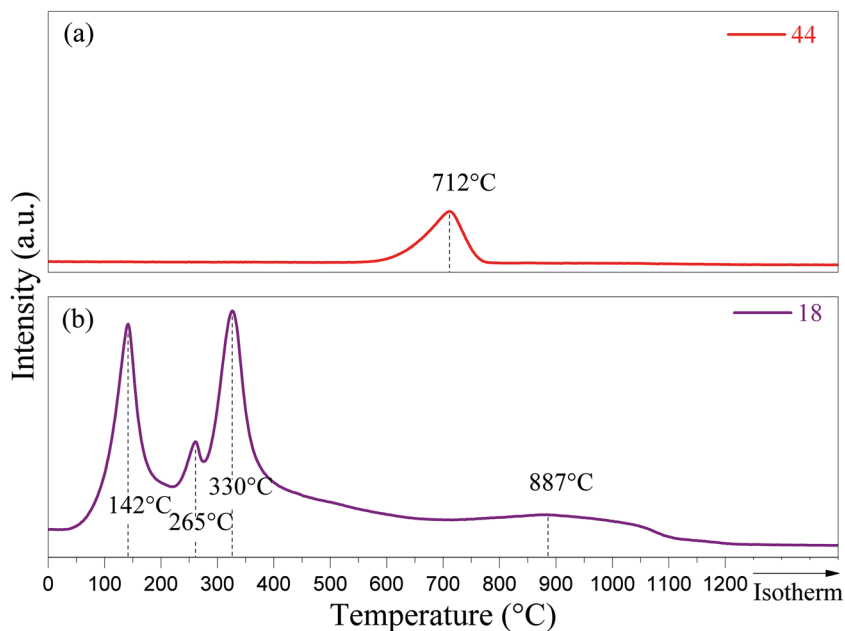
Fig. 9. Mass spectrometry analysis of sample HC36H65D for m/e of **a** 44 and **b** 18

HC36H95D absorbed the largest amount of heat to decompose the carbonate to CO_2 (971 kJ kg^{-1}), which led to the belief that CO_2 interacted most strongly with the material structure.

Chloride decomposition as hydrochloric acid is exothermic; hence, the negative signal (Table 6) was related to the heat associated with stages 5 and 4 (HC36H95D) and the upward peak (Fig. 8). The heat of chloride decomposition varied from –4708 to –7197 kJ kg^{-1} (Table 6). Because sample HC9H35D

released the greatest heat of decomposition, the chloride in this sample probably interacted more strongly with the hydrocalumite structure. Prado et al. (2016) observed only a slight mass loss during the exothermic event above 750°C. On the other hand, when the temperature approached 1200°C the mass loss increased. They also reported that between 800 and 1200°C the mass variation was small (2.7 wt.%) and slow, so the mass spectrometer could not detect the
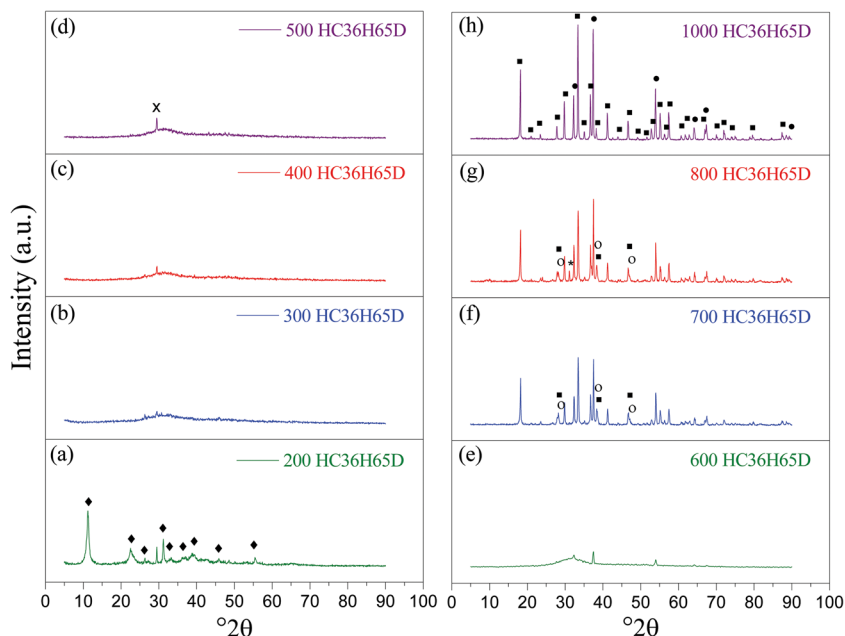
Fig. 10. XRD patterns for sample HC36H65D calcined at **a** 200°C, **b** 300°C, **c** 400°C, **d** 500°C, **e** 600°C, **f** 700°C, **g** 800°C, and **h** 1000°C. ♦ – $Ca_4Al_2O_6Cl_2·10H_2O$, X – $CaCO_3$, ● – CaO, ■ – $Ca_{12}Al_{14}O_{33}$, o – CaClOH, and * – unknown
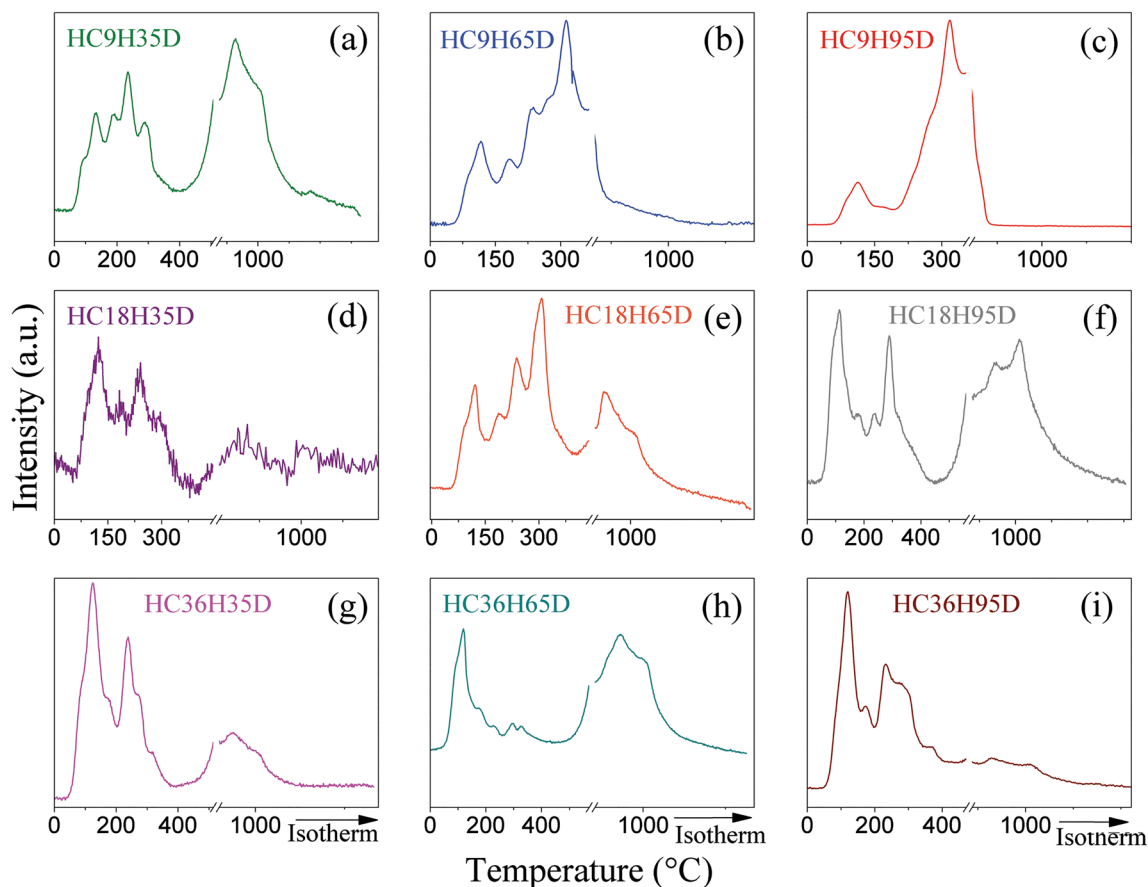
Fig. 11. CO₂ temperature-programmed desorption profiles (TPD-CO₂) showing the peaks of low intensity for the samples: **a–c** 9 h, **d–f** 18 h, and **g–i** 36 h

decomposed chemical species. The total mass loss was ~39 wt.% (Prado et al. 2016). Results from the present study confirm the observations by Prado et al. (2016) that the final mass loss was also exothermic with slight mass loss.

Changes in structure due to heat treatments were measured by XRD (Fig. 10). Sample HC36H65D was used as a representative hydrocalumite sample and was heated in a TGA under 60 mL min⁻¹ air flow to 200, 300, 400, 500, 600, 700, 800, or 1000°C, then cooled. The XRD pattern from 200°C treatment revealed that the hydrocalumite structure was not destroyed, but became less crystalline (broader XRD peaks). At 300°C, the hydrocalumite structure was completely destroyed, with the formation of an amorphous material (shoulder at 30°2θ). A similar result was obtained after the 400 and 500°C treatments. As previously mentioned, the sample was carbonated, so a very small peak due to $CaCO_3$ formation was observed.

At 600°C, low-intensity peaks assigned to lime (CaO) were formed and the shoulder at 30°2θ remained (Fig. 10); thus, the calcite was completely decomposed at this temperature. At 700°C, a phase mixture composed of mayenite ($Ca_{12}Al_{14}O_{33}$), lime, and calcium chloride hydroxide (CaClOH) was formed, in which the major peaks

of mayenite (33.4°2θ) and lime (37.3°2θ) were of similar intensity. The XRD pattern of the sample heated at 800°C was similar to that calcined at 700°C, but the main lime peak was slightly larger than that of mayenite. In addition, an unknown phase was observed near 31°2θ. At 1000°C, the solid mixture was composed of mayenite and lime and the CaClOH phase disappeared, which corroborated the thermogravimetric analysis result, i.e. that chlorine was released from the sample between 1000 and 1200°C. The main mayenite and lime peaks were of similar intensity. The peak intensity increased from 700 to 1000°C, reflecting the greater crystallinity of the material.

Domínguez et al. (2011) studied hydrocalumite calcination at 500 and 900°C, and reported an amorphous phase without identification after 500°C heat treatment of a mixture of CaO, $Ca_{12}Al_{14}O_{33}$, and CaClOH at 900°C. Kuwahara et al. (2012) calcined hydrocalumite to study the material structure. At 400°C, the lamellar structure collapsed, showing a broad peak near 30°2θ (visualized by XRD). This structure was characteristic of an amorphous phase which may be calcium and aluminum mixed oxide. Calcination at 600 and 800°C transformed the material structure into a mixture of lime and mayenite; in addition, the XRD peak intensity increased. The XRD
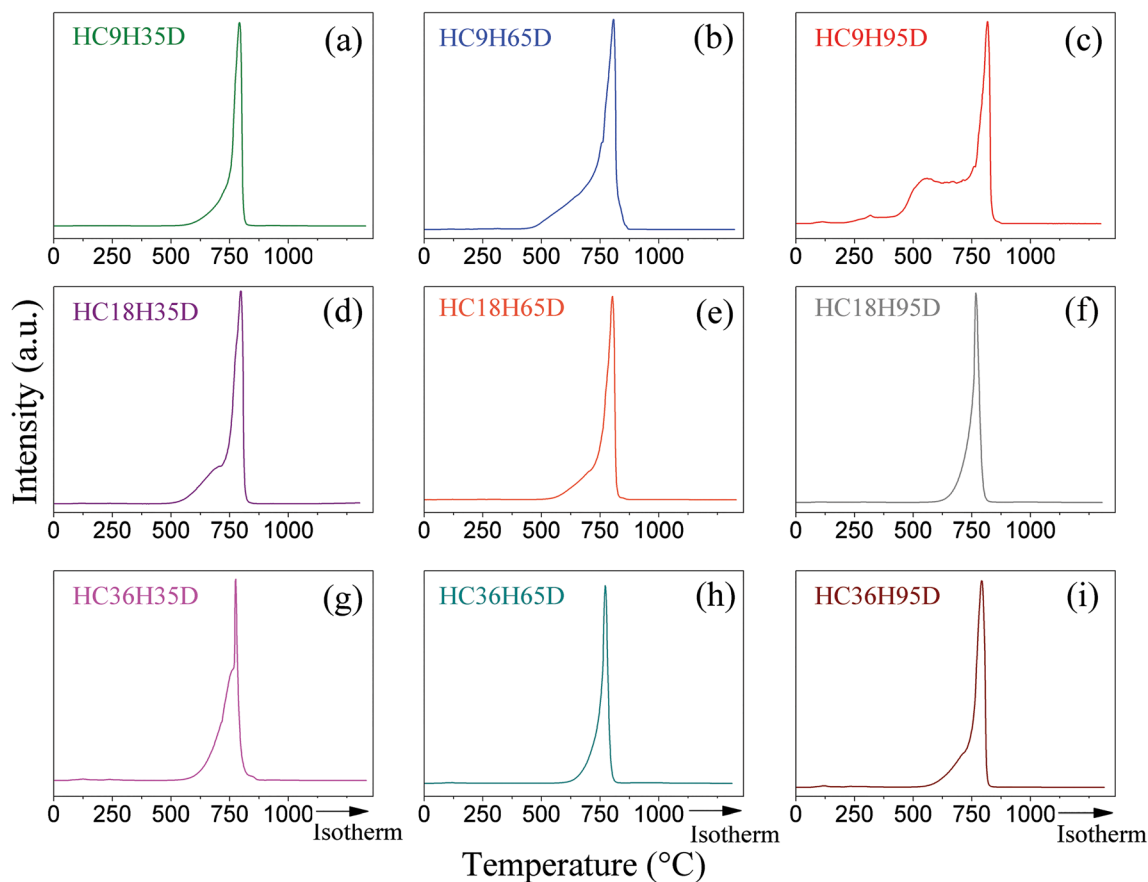
Fig. 12. CO$_2$ temperature-programmed desorption profiles (TPD-CO$_2$) showing the peaks of high intensity for the samples: **a–c** 9 h, **d–f** 18 h, and **g–i** 36 h

pattern of samples calcined at 1000°C was similar to that at 800°C. These observations confirmed those of Kuwahara et al. (2012).

The results achieved during the present study confirmed the observations of Prado et al. (2016) that hydrocalumite dehydrates up to 190°C, then partially dehydroxylates up to 570°C. The XRD profiles of samples calcined at 500°C showed the existence of an amorphous phase and crystalline CaCO$_3$. At 700°C, the CaCO$_3$ was converted to CaO, and between 570 and 750°C the decarbonation was responsible for the mass loss as the CO$_2$ signal was verified by MS (m/e = 44). In the sample

Table 7. CO$_2$ temperature programmed desorption (TPD-CO$_2$): total amount and distribution of basic sites

Sample	Total basic sites (µmol g^{-1})	Basic site distribution[a] (µmol g^{-1})		
		Weak	Moderate	Strong
HC9H35D	1344	3(0.2)	3(0.2)	1338(99.6)
HC9H65D	1557	3(0.2)	10(0.6)	1544(99.2)
HC9H95D	594	3(0.5)	19(3.2)	572(96.3)
HC18H35D	1031	5(0.5)	1(0.1)	1025(99.4)
HC18H65D	1502	3(0.2)	5(0.4)	1494(99.4)
HC18H95D	571	3(0.4)	2(0.4)	566(99.2)
HC36H35D	337	5(1.4)	1(0.4)	331(98.2)
HC36H65D	668	7(1.0)	1(0.1)	660(98.9)
HC36H95D	530	7(1.3)	4(0.8)	519(97.9)

[a] The number in parentheses is the corresponding percentage of total amount of basic sites.

heated at 750°C, the XRD profiles showed CaO and $Ca_{12}Al_{14}O_{33}$ crystalline phases. Chloride was decomposed as HCl between 830 and 1000°C (Prado et al. 2016).

CO_2-TPD profiles revealed low-intensity peaks from CO_2 desorption peaks in the temperature ranges of 100–400°C and 900–1000°C (Fig. 11) and high-intensity peaks between 500–800°C (Fig. 12). The larger peaks were plotted separately so as not to hinder the visualization of the smaller peaks. The basic sites were classified according to their basicity: desorption peaks between (1) 100–250°C – weak, (2) 250–500°C – moderate, and (3) >500°C – strong. According to Kuwahara et al. (2012), hydrocalumites contain basic sites, as demonstrated by weak TPD-CO_2 peaks at 97°C and moderate TPD-CO_2 peaks at 298°C. The weak sites are attributed to surface hydroxyls and the moderate ones to O^{2-} ions adjacent to the hydroxyls.

Quantification of the basic sites (Table 7) showed that hydrocalumites were composed mainly of strong basic sites. Samples aged for 9 h had a larger amount of total basic sites, i.e. the increase in aging time reduced basicity, with the largest number occurring at the aging temperature of 65°C and the smaller number at 95°C, except for sample HC36H95D.

CONCLUSIONS

Characterization of hydrocalumites synthesized by the coprecipitation method under various aging conditions revealed that this method is suitable for the production of pure and crystalline layered double hydroxide with a Ca/Al molar ratio of 2. The water/ethanol mixture used in the synthesis prevented sample poisoning by atmospheric carbon dioxide. The variation of aging time and temperature promoted changes in the structure, textural properties, morphology, thermal stability, and basicity of hydrocalumite. Aging at 95°C was decisive for providing more crystalline samples, and aging for 36 h was best to yield hydrocalumites with larger surface areas (up to 20.2 m^2 g^{-1}). Aging at 65°C for 9 h was the optimum condition to maximize the hydrocalumite basicity (1557 μmol g^{-1}).

ACKNOWLEDGMENTS

Compliance with ethical standards

Conflict of Interest
The authors declare that they have no conflict of interest.

REFERENCES

Barrado, E.P. (2015). Layered double hydroxides for applications in catalysis and electroluminescent devices. PhD thesis, Universitat Rovira I Virgili, 189 pp.

Cavani, F., Trifirò, F., & Vaccari, A. (1991). Hydrotalcite-type anionic clays: preparation, properties and applications. *Catalysis Today, 11*, 173–301.

Chen, H., Sun, Y., Ruan, X., Yu, Y., Zhu, M., Zhang, J., Zhou, J., Xu, Y., Liu, J., & Qian, G. (2016). Advanced treatment of stabilized landfill leachate after biochemical process with hydrocalumite chloride (Ca/Al-Cl LDH). *Bioresource Technology, 210*, 131–137.

Cota, I., Ramírez, E., Medina, F., Sueiras, J. E., Layrac, G., & Tichit, D. (2010). New synthesis route of hydrocalumite-type materials and their application as basic catalysts for aldol condensation. *Applied Clay Science, 50*, 498–502.

Domínguez, M., Pérez-Bernal, M. E., Ruano-Casero, R. J., Barriga, C., Rives, V., Ferreira, R. A. S., Carlos, L. D., & Rocha, J. (2011). Multiwavelength luminescence in lanthanide-doped hydrocalumite and mayenite. *Chemistry of Materials, 23*, 1993–2004.

Granados-Reyes, J., Salagre, P., & Cesteros, Y. (2014). Effect of microwaves, ultrasounds and interlayer anion on the hydrocalumites synthesis. *Microporous and Mesoporous Materials, 199*, 117–124.

Guo, Q., & Tian, J. (2013). Removal of fluoride and arsenate from aqueous solution by hydrocalumite via precipitation and anion exchange. *Chemical Engineering Journal, 231*, 121–131.

Hills, A. W. D. (1968). The mechanism of the thermal decomposition of calcium carbonate. *Chemical Engineering Science, 23*, 297–320.

Jia, Y., Wang, H., Zhao, X., Liu, X., Wang, Y., Fan, Q., & Zhou, J. (2016). Kinetics, isotherms and multiple mechanisms of the removal for phosphate by Cl-hydrocalumite. *Applied Clay Science, 129*, 116–121.

Kuwahara, Y., Tsuji, K., Ohmichi, T., Kamegawa, T., Mori, K., & Yamashita, H. (2012). Waste-slag hydrocalumite and derivatives as heterogeneous base catalysts. *ChemSusChem, 5*, 1523–1532.

Leroux, F., Léone, P., Besse, J.-P., Taviot-Guého, C., Palvadeau, P., & Rousselot, I. (2002). Insights on the structural chemistry of hydrocalumite and hydrotalcite-like materials: investigation of the series $Ca_2M^{3+}(OH)_6Cl\cdot2H_2O$ (M^{3+}: Al^{3+}, Ga^{3+}, Fe^{3+}, and Sc^{3+}) by X-Ray Powder Diffraction. *Journal of Solid State Chemistry, 167*, 137–144.

Linares, C. F., Ocanto, F., Bretto, P., & Monsalve, M. (2014). Study of as-synthesized and calcined hydrocalumites as possible antacid agents. *Bulletin of Materials Science, 37*, 941–944.

Linares, C. F., Moscosso, J., Alzurutt, V., Ocanto, F., Bretto, P., & González, G. (2016). Carbonated hydrocalumite synthesized by the microwave method as a possible antacid. *Materials Science and Engineering C, 61*, 875–878.

López-Salinas, E., Serrano, M. E. L., Jácome, M. A. C., & Secora, I. S. (1996). Characterization of synthetic hydrocalumite-type $[Ca_2Al(OH)_6]NO_3\cdot mH_2O$: Effect of the calcination temperature. *Journal of Porous Materials, 2*, 291–297.

Mao, N., Zhou, C. H., Tong, D. S., Yu, W. H., & Lin, C. X. C. (2017). Exfoliation of layered double hydroxide solids into functional nanosheets. *Applied Clay Science, 144*, 60–78.

Mao, N., Zhou, C. H., Keeling, J., Fiore, S., Zhang, H., Chen, L., Jin, G. C., Zhu, T. T., Tong, D. S., & Yu, W. H. (2018). Tracked changes of dolomite into Ca-Mg-Al layered double hydroxide. *Applied Clay Science, 159*, 25–36.

Marsal, L. F., Salagre, P., Díaz, F., Cesteros, Y., Pérez-Barrado, E., Aguiló, M., Llorca, J., Pujol, M. C., & Pallarès, J. (2015). Influence of acid–base properties of calcined MgAl and CaAl layered double hydroxides on the catalytic glycerol etherification to short-chain polyglycerols. *Chemical Engineering Journal, 264*, 547–556.

Oladoja, N. A., Adelagun, R. O. A., Ololade, I. A., Anthony, E. T., & Alfred, M. O. (2014). Synthesis of nano-sized hydrocalumite from a Gastropod shell for aqua system phosphate removal. *Separation and Purification Technology, 124*, 186–194.

Pérez-Barrado, E., Pujol, M. C., Aguiló, M., Cesteros, Y., Díaz, F., Pallarès, J., Marsal, L. F., & Salagre, P. (2013). Fast aging treatment for the synthesis of hydrocalumites using microwaves. *Applied Clay Science, 80–81*, 313–319.

Pfeiffer, H., Ávalos-Rendón, T., Lima, E., & Valente, J. S. (2011). Thermochemical and cyclability analyses of the CO_2 absorption

process on a Ca/Al layered double hydroxide. *Journal of Environmental Engineering, 137*, 1058–1065.

Prado, R. G., Almeida, G. D., De Oliveira, A. R., De Souza, P. M. T. G., Cardoso, C. C., Constantino, V. R. L., Pinto, F. G., Tronto, J., & Pasa, V. M. D. (2016). Ethanolysis and methanolysis of soybean and macauba oils catalyzed by mixed oxide Ca-Al from hydrocalumite for biodiesel production. *Energy and Fuels, 30*, 6662–6670.

Rossi, T. M., Campos, J. C., & Souza, M. M. V. M. (2019). An evaluation of calcined hydrocalumite as carbon dioxide adsorbent using thermogravimetric analysis. *Applied Clay Science, 182*, 105252–105261.

Roy, A., Forano, C., Malki, K. E., & Besse, J. P. (1992). Anionic clays: trends in pillaring chemistry. *Expanded Clays and Other Microporous Solids, 2*, 108–169.

Sánchez-Cantú, M., Camargo-Martínez, S., Pérez-Díaz, L. M., Hernández-Torres, M. E., Rubio-Rosas, E., & Valente, J. S. (2015). Innovative method for hydrocalumite-like compounds' preparation and their evaluation in the transesterification reaction. *Applied Clay Science, 114*, 509–516.

Sánchez-Cantú, M., Barcelos-Santiago, C., Gomez, C. M., Ramos-Ramírez, E., Ruiz Peralta, M. d. L., Tepale, N., González-Coronel, V. J., Mantilla, A., & Tzompantzi, F. (2016). Evaluation of hydrocalumite-like compounds as catalyst precursors in the photodegradation of 2,4-dichlorophenoxyacetic acid. *International Journal of Photoenergy, 2016*, 1–13.

Terzis, A., Filippakis, S., Kuzel, H. J., & Burzlaff, H. (1987). The crystal structure of $Ca_2Al(OH)_6Cl.2H_2O$. *Zeitschrift für Kristallographie - Crystalline Materials, 181*, 29–34.

Wen, X., Yang, Z., Yan, J., & Xie, X. (2015). Green preparation and characterization of a novel heat stabilizer for poly(vinyl chloride)-hydrocalumites. *RSC Advances, 5*, 32020–32026.

Wen, X., Yang, Z., Xiao, X., Yang, H., Xie, X., & Huang, J. (2016). The impact of hydrocalumites additives on the electrochemical performance of zinc-nickel secondary cells. *Electrochimica Acta, 187*, 65–72.

Wu, Y., Chi, Y., Bai, H., Qian, G., Cao, Y., Zhou, J., Xu, Y., Liu, Q., Xu, Z. P., & Qiao, S. (2010). Effective removal of selenate from aqueous solutions by the Friedel phase. *Journal of Hazardous Materials, 176*, 193–198.

Xu, S., Zhang, B., Chen, Z., Yu, J., Evans, D. G., & Zhang, F. (2011). A general and scalable formulation of pure CaAl-layered double hydroxide via an organic/water solution route. *Industrial and Engineering Chemistry Research, 50*, 6567–6572.

Zhang, P., Qian, G., Shi, H., Ruan, X., Yang, J., & Frost, R. L. (2012). Mechanism of interaction of hydrocalumites (Ca/Al-LDH) with methyl orange and acidic scarlet GR. *Journal of Colloid and Interface Science, 365*, 110–116.